

Cascade of transitions between the correlated electronic states of magic-angle twisted bilayer graphene

Dillon Wong^{1,*}, Kevin P. Nuckolls^{1,*}, Myungchul Oh^{1,*}, Biao Lian^{2,*}, Yonglong Xie^{1,†}, Sangjun Jeon^{1,#}, Kenji Watanabe³, Takashi Taniguchi³, B. Andrei Bernevig², and Ali Yazdani^{1,‡}

¹*Joseph Henry Laboratories & Department of Physics, Princeton University, Princeton, NJ 08544, USA*

²*Princeton Center for Theoretical Science, Princeton University, Princeton, New Jersey 08544, USA*

³*National Institute for Material Science, 1-1 Namiki, Tsukuba 305-0044, Japan*

* These authors contributed equally to this work.

† Present Address: Department of Physics, Harvard University, Cambridge, MA 02138, USA

Present Address: Department of Physics, Chung-Ang University, Seoul 06974, Republic of Korea

‡ email: yazdani@princeton.edu

Magic-angle twisted bilayer graphene (MATBG) exhibits a rich variety of electronic states, including correlated insulators¹⁻³, superconductors²⁻⁴, and topological phases^{3,5,6}.

Understanding the microscopic mechanisms responsible for these phases requires determining the interplay between electron-electron interactions and quantum degeneracy due to spin and valley degrees of freedom. Signatures of strong electron-electron correlations have been observed at partial fillings of the flat electronic bands in recent spectroscopic measurements⁷⁻¹⁰. Transport experiments in a magnetic field show changes in the degeneracy of the Landau levels (LL) at fillings corresponding to an integer number of electrons per moiré unit cell²⁻⁴. However, the interplay between interaction effects and the quantum degeneracy of the system is currently unclear. Using high-resolution scanning tunneling microscopy (STM), we observed a cascade of transitions in the spectroscopic properties of MATBG as a function of electron filling. We find distinct changes in the chemical potential and a rearrangement of the low-energy excitations at each integer filling

of the moiré flat bands. These spectroscopic features are a direct consequence of Coulomb interactions, which split the degenerate flat bands into Hubbard sub-bands. We find these interactions, the strength of which we can extract experimentally, to be surprisingly sensitive to the presence of a perpendicular magnetic field, which strongly modifies the spectroscopic transitions. The cascade of transitions we report here characterizes the correlated high-temperature parent phase^{11,12} from which various insulating and superconducting ground-state phases emerge at low temperatures in MATBG.

Stacks of two-dimensional (2D) van der Waals monolayers represent a new material platform for the realization of correlated and topological electronic states. By twisting 2D atomic crystals relative to each other, it is possible to form a moiré superlattice structure with electronic bandwidth that is comparable in energy to that of Coulomb interactions, thereby creating the conditions for the formation of correlated phases^{1,2,20,4,13–19}. Recent discoveries of various electronic phases in MATBG have occurred precisely in this regime, where band structure calculations show the formation of two nearly flat bands near charge neutrality^{21–25}, while estimates for the Coulomb interaction for electrons separated by the moiré superlattice spacing yield an energy comparable to or larger than the expected flat bands' bandwidth^{26,27}. Consistent with this picture, previous STM measurements have shown signatures of many-body correlations in this system^{7–10}. Spectroscopy at densities where the flat bands are fully occupied or fully empty show sharp van Hove singularities (vHs) associated with nearly flat conduction and valence bands, while spectra of partially occupied flat bands show a dramatic broadening of both bands, indicating the importance of interaction-induced charge fluctuations⁷. Here we show that in this highly correlated precursor state, there exist successions of spectroscopic transitions at every integer filling of both the conduction and valence flat bands. An analysis of these

spectroscopic data based on a Hubbard-model picture of its electronic states provides a direct measurement of the Coulomb repulsion strength U and uncovers signatures of sharp transitions in the chemical potential of this system at every integer filling. Our results demonstrate the natural influence of spin and valley degeneracies on the electronic properties of this strongly interacting system.

A schematic of our experimental setup is shown in Fig. 1a. MATBG samples were prepared on exfoliated boron nitride (h-BN) using the “tear-and-stack” technique²⁸ (see Methods) and were electrically contacted via Ti/Au electrodes on SiO₂/Si substrates. Our devices were studied in a homebuilt STM system²⁹, biased at V_b relative to a tungsten tip, and gated with a voltage V_g applied to Si. An STM topograph of a typical device shown in Fig. 1b displays three coexisting lattices: the graphene atomic lattice, a moiré pattern of size $\lambda_{g-BN} \approx 1.76$ nm (8°) due to misalignment of the graphene and the h-BN substrate, and a moiré pattern of size $\lambda_{g-g} \approx 13.3$ nm (1.06° , 0.1% interlayer relative strain) due to the misalignment of the top and bottom graphene layers. The bright regions in the STM images correspond to the AA stacking regions of MATBG^{30–32}, at the center of which the differential conductance (dI/dV) shows the vHs of the flat bands appearing as two peaks whose energy locations and widths depend on the carrier density (see Extended Data Fig. 1 for dI/dV curves).

A cascade of changes in the electronic properties of MATBG are observed in high-resolution STM spectra measured at the center of each AA site as a function of V_g (Fig. 1c), which tunes the electron filling $\nu = \pm n/n_0$, where $\nu = \pm 4$ corresponds to the fully occupied/empty fourfold-degenerate (spin/valley) flat bands around charge neutrality. As found in previous studies^{7–9}, the vHs of the two flat bands appear as two sharp, parallel lines in $dI/dV(V_b, V_g)$ when both flat bands are fully occupied ($V_g > 40$ V) or full empty ($V_g < -40$ V). In this region, dI/dV is

consistent with non-interacting models of the band structure of MATBG^{21–24}. At $\nu = \pm 4$, when the chemical potential is tuned across the gap from either of the remote bands into either of the flat bands, the spectra show an immediate broadening of the flat bands, which has previously been shown to be a consequence of strong electronic interactions in this system⁷. This broadening is accompanied by a sequence of previously unresolved finer features around the Fermi energy (E_F) (Fig. 1c). Division of dI/dV by I/V_b , typically used when there are large variations of the tunneling current as a function of bias, more clearly displays these finer features in the spectroscopy of MATBG as a function of carrier density (Fig. 1d). The cascade of features we observe around E_F repeats in four evenly spaced intervals between $\nu = +4$ and the charge neutrality point (CNP) at $\nu = 0$, and in four more intervals before the chemical potential is tuned below the flat bands and into the valence remote band at filling $\nu = -4$. The 14 features seen in spectroscopy around E_F , schematically sketched in Fig. 1e, show systematic variations with V_b as a function of electron filling. Each unfilled excitation ($V_b > 0$ V) appears first at E_F and disperses outwards with decreasing ν to energies of about 23 meV before disappearing. The features near the CNP disperse to higher energies, pushed further by the energy between the flat bands. In contrast, each filled excitation ($V_b < 0$ V) is first detected at negative bias and moves closer to E_F with decreasing ν (Figs. 1c-f). Extended Data Fig. 2 shows more dI/dV data, acquired on AA sites in twisted regions within 0.1° of the magic angle, containing features with similar behavior.

A starting point for understanding the sequence of features in our spectroscopic measurements is to consider a model consisting of two perfectly flat bands separated by energy $2E_0$, each with four internal degrees of freedom (“flavors”) due to the spin and valley degeneracies, and an on-site Hubbard interaction energy U describing the Coulomb repulsion between electrons (Fig. 2a). As described below, our data suggests that in a more realistic

picture, these bands are not perfectly flat, and there is a small but finite density of states (DOS) in between the flat bands (potentially from Dirac nodes expected in MATBG's band structure). However, this simple Hubbard-model picture in the limit of vanishing hopping provides a natural way to understand our observed spectroscopic features. In Fig. 2a, we see that there are sudden changes in the spectral weight corresponding to adding and removing an electron at integer values of ν . Furthermore, in this simple model, there are also jumps in the chemical potential at integer ν (Fig. 2d) equal to the on-site Hubbard energy U (except at the CNP where the chemical potential jumps by $2E_0 + U$).

The features in the calculated spectral weight in Fig. 2a arise from one-particle excitations from nine types of minimum-energy states schematically depicted in Fig. 2b. The red (blue) ovals represent the conduction (valence) flat band, each colored circle represents an electron of a specific flavor, and each arrow represents a possible excitation from this minimum-energy state and its corresponding energetic cost. Together, these excitations give rise to the "Hubbard sub-bands" drawn in Fig. 2c whose spectroscopic degeneracy is given by the number of ways an electron can be added to or removed from a minimum-energy state. The on-site repulsion U separates each of the fourfold-degenerate flat bands into Hubbard sub-bands, even in the absence of any symmetry-breaking effects. Within this picture, the features corresponding to electron addition excitations peel away from E_F between integer fillings, reaching a maximum energy of U before losing intensity. The spectral weight beyond energy U is generically from one-particle excitations of higher-energy on-site electron configurations and is exponentially suppressed (See Methods for details). Near the CNP, the features corresponding to electron addition or removal include, in addition to U , the energy separation between the flat bands, causing them to extend to a maximum energy of $\pm(2E_0 + U)$. This enhanced flat band separation

is consistent with the features seen in Figs. 1c-d near $V_g = 0$ V, which extend to higher biases than those seen at other filling values.

There are a few key differences between this perfectly flat band Hubbard model and our observations. First, from our spectroscopic measurements we expect the two flat bands to have finite bandwidths with a small but finite DOS in between the bands. This would cause the cascading features in the spectra to disperse at intermediate fillings instead of being pinned at E_F and suddenly jumping at integer values of ν , which is more consistent with the experimental observations. An exact diagonalization study, which includes a finite hopping term in addition to on-site U , clearly demonstrates this behavior (see Extended Data Fig. 3). Second, the electric field caused by both the bias voltage and the difference between the work functions of the STM tip and sample causes local band bending and charging effects, slightly shifting some of the features in Fig. 1c from the idealized picture in Fig. 2a⁷.

From the correspondence drawn between the sequence of features in our data and the excitation spectrum expected from a Hubbard model with fourfold degeneracy, we extract a measure of the on-site Coulomb repulsion strength $U = 23 \pm 5$ meV, consistent with previous estimates⁷. This value of U is much larger than non-interacting estimates for both the bandwidth of a flat band and the energy separation between two flat bands^{21–24}, both of which we have also experimentally resolved in the non-interacting regime ($V_g > 40$ V in Fig. 1c). This relation inverts for twist angles both larger and smaller than the magic angle, where the electronic bandwidth becomes comparable to or larger than the Hubbard interaction energy. In this regime, for twisted bilayer graphene at angles 0.85° and 1.21° , we find no evidence of the cascades in spectra as a function of electron filling, despite the presence of strong E_F pinning behavior (see

Extended Data Fig. 4). This confirms the lack of well-defined Hubbard sub-bands when U is no longer the largest energy scale.

The flavor-induced reorganization of electronic states in MATBG can also be seen in the gate dependence of the spectroscopic behavior of the remote bands nearest to the flat bands, from which we can extract information regarding changes in the system's chemical potential as a function of carrier density. To probe the remote bands, we perform dI/dV measurements at the center of the AB/BA regions (Fig. 3a; 1.05° , 0.2% strain; see Extended Data Fig. 5 for dI/dV curves), where the flat bands' contribution to the spectral weight no longer dominates the measurements. At these locations, the spectra provide information that is more sensitive to the delocalized states of MATBG and their carrier-density-dependent interactions with the flat bands. The edge of the conduction remote band, with onset energy $E_{R+}(\nu)$ (37.5 meV at $\nu = +4$), and the valence remote band, with onset energy $E_{R-}(\nu)$ (-79.5 meV at $\nu = +4$), show a periodic modulation as a function of carrier density that is in-phase with integer fillings of the flat bands (Figs. 3a, c). Such behavior is most clearly resolved in the conduction remote band above the CNP.

To understand the gate-dependent periodicity of the remote band onsets, we consider a simple mean-field interaction model $E_{R+(-)}(\nu) = \Delta_{R+(-)} + \nu U' - \mu(\nu)$, where $\Delta_{R+(-)}$ is the energy difference between the flat bands and the conduction (valence) remote band in the absence of any interactions, $\nu U'$ is a mean-field term describing the interactions between electrons in the flat bands and an electron in the remote band (the mean-field approximation is justified because the remote bands are delocalized), and $\mu(\nu)$ is the chemical potential of the system at filling ν . We use this form for $E_{R+(-)}(\nu)$ to extract the interaction strength U' from the data in Fig. 3a and determine the behavior of $\mu(\nu)$ (see Methods for details). The results, shown in Fig. 3d, illustrate

that while $\mu(\nu)$ does not jump as a function of ν as we expect for our simple Hubbard model (Fig. 2d and Extended Data Fig. 3b), $\mu(\nu)$ shows distinct cusps at every integer filling. The difference lies in the fact that, at integer fillings, our simple Hubbard model in the limit of U much greater than the bandwidth W is a Mott insulator, which has a charge gap of size $U-W$ at E_F . In contrast, our measurements at these high temperatures ($T \approx 6$ K) do not yet show any hard charge gaps at E_F , indicating a finite DOS between the flat bands. This finite DOS could be associated with, for example, the tails of the flat bands or a high-velocity Dirac point in between these bands. The cusps in $\mu(\nu)$ at integer values of ν also coincide with non-zero dips in the DOS at E_F that can be seen in the plot of $dI/dV(V_b = 0$ V) as a function of V_g (Fig. 3e). Moreover, each cusp forms at the junctions of two asymmetric slopes of $\mu(\nu)$, which is consistent with differences in the DOS between the top and bottom of sequential Hubbard sub-bands (schematically depicted in Fig. 2c). Our measurements of cusps in $\mu(\nu)$ imply a sudden drop in the compressibility and the cyclotron effective mass when increasing (decreasing) the charge carrier density across a positive (negative) integer value of ν . Since energetically well-separated Landau levels require low cyclotron masses, this observation may explain the unusual asymmetry in the Landau fans seen near non-zero integer fillings in transport studies²⁻⁴.

We have thus far only invoked a local picture of the Coulomb interaction, motivated by the experimental observation that the flat bands' electronic states are mostly spatially localized to the AA sites. Such a local picture with a large Hubbard interaction energy is adequate for understanding most of our findings, yet fails to explain the behavior of our system in the presence of a large magnetic field. Surprisingly, we find that application of an out-of-plane magnetic field of 9 T (at temperature $T \approx 6$ K) strongly modifies the observed zero-field cascades and suppresses both the cusp-like behavior of $\mu(\nu)$ at integer ν and the dips in the DOS at E_F

(Fig. 3b, e). A large response to low magnetic fields has been predicted to arise from coupling to the magnetic moment of moiré-scale orbital current loops, which would form due to valley polarization^{33–35}; however, the relationship between our measurements and these proposed ground states is not clear. This remarkable sensitivity to a perpendicular magnetic field, in which changes in the system’s degeneracy have also been detected in lower-temperature transport studies^{2–4}, cannot be understood with our local picture. The experimental data suggest that the application of a perpendicular magnetic field of this magnitude may actually delocalize some electrons within the flat bands from the confinement of the moiré superlattice structure, which would result in an apparent suppression of the effective local interaction strength U that drives the cascade of transitions and remote band oscillations that we have uncovered at zero magnetic field.

Further measurements are required to fully establish the connection between our high-temperature observations of the restructuring of low-energy excitations, the cusps in $\mu(\nu)$, and the suppression of DOS at E_F at each integer filling to the formation of insulating and magnetic phases reported in transport studies at low temperatures ($T < 5$ K)^{1–4}. Our experiments show that even at high temperatures, interactions separate the flat bands of MATBG into several Hubbard sub-bands. This could further drive the formation of long-range flavor-polarized insulating or magnetic ground states at low temperatures, as several theoretical studies suggest^{26,36}. However, the presence of strong interactions may also cause the spontaneous breaking of other symmetries to create insulating or semi-metallic phases different from those with purely spin/valley flavor polarization²⁴. More broadly, we speculate that similar cascades of electronic transitions may occur in other moiré flat band systems made from 2D crystals other than graphene, where local electronic interaction effects are dominant and internal quantum degrees of freedom are present.

References

1. Cao, Y. *et al.* Correlated insulator behaviour at half-filling in magic-angle graphene superlattices. *Nature* **556**, 80–84 (2018).
2. Yankowitz, M. *et al.* Tuning superconductivity in twisted bilayer graphene. *Science* **363**, 1059–1064 (2019).
3. Lu, X. *et al.* Superconductors, orbital magnets, and correlated states in magic-angle bilayer graphene. *Nature* **574**, 20–23 (2019).
4. Cao, Y. *et al.* Unconventional superconductivity in magic-angle graphene superlattices. *Nature* **556**, 43–50 (2018).
5. Sharpe, A. L. *et al.* Emergent ferromagnetism near three-quarters filling in twisted bilayer graphene. *Science* **365**, 605–608 (2019).
6. Serlin, M. *et al.* Intrinsic quantized anomalous Hall effect in a moiré heterostructure. Preprint at <https://arxiv.org/abs/1907.00261> (2019).
7. Xie, Y. *et al.* Spectroscopic signatures of many-body correlations in magic-angle twisted bilayer graphene. *Nature* **572**, 101–105 (2019).
8. Kerelsky, A. *et al.* Maximized electron interactions at the magic angle in twisted bilayer graphene. *Nature* **572**, 95–100 (2019).
9. Choi, Y. *et al.* Electronic correlations in twisted bilayer graphene near the magic angle. *Nat. Phys.* (2019). doi:10.1038/s41567-019-0606-5
10. Jiang, Y. *et al.* Charge order and broken rotational symmetry in magic-angle twisted bilayer graphene. *Nature* **573**, 91–95 (2019).
11. Cao, Y. *et al.* Strange metal in magic-angle graphene with near Planckian dissipation. Preprint at <https://arxiv.org/abs/1901.03710> (2019).
12. Polshyn, H. *et al.* Large linear-in-temperature resistivity in twisted bilayer graphene. *Nat. Phys.* **15**, 1011–1016 (2019).
13. Chen, G. *et al.* Signatures of tunable superconductivity in a trilayer graphene moiré superlattice. *Nature* **572**, 215–219 (2019).
14. Cao, Y. *et al.* Electric Field Tunable Correlated States and Magnetic Phase Transitions in Twisted Bilayer-Bilayer Graphene. Preprint at <http://arxiv.org/abs/1903.08596> (2019).
15. Liu, X. *et al.* Spin-polarized Correlated Insulator and Superconductor in Twisted Double Bilayer Graphene. Preprint at <https://arxiv.org/abs/1903.08130> (2019).
16. Shen, C. *et al.* Observation of superconductivity with T_c onset at 12K in electrically tunable twisted double bilayer graphene. Preprint at <https://arxiv.org/abs/1903.06952> (2019).
17. Regan, E. C. *et al.* Optical detection of Mott and generalized Wigner crystal states in WSe₂/WS₂ moiré superlattices. Preprint at <https://arxiv.org/abs/1910.09047> (2019).
18. Tang, Y. *et al.* WSe₂/WS₂ moiré superlattices: a new Hubbard model simulator. Preprint

- at <https://arxiv.org/abs/1910.08673> (2019).
19. Wang, L. *et al.* Magic continuum in twisted bilayer WSe₂. Preprint at <https://arxiv.org/abs/1910.12147> (2019).
 20. Chen, G. *et al.* Tunable Correlated Chern Insulator and Ferromagnetism in Trilayer Graphene/Boron Nitride Moiré Superlattice. Preprint at <https://arxiv.org/abs/1905.06535> (2019).
 21. Bistritzer, R. & MacDonald, A. H. Moiré bands in twisted double-layer graphene. *Proc. Natl. Acad. Sci. U. S. A.* **108**, 12233–12237 (2011).
 22. Carr, S., Fang, S., Zhu, Z. & Kaxiras, E. Exact continuum model for low-energy electronic states of twisted bilayer graphene. *Phys. Rev. Res.* **1**, 1–6 (2019).
 23. Koshino, M. *et al.* Maximally Localized Wannier Orbitals and the Extended Hubbard Model for Twisted Bilayer Graphene. *Phys. Rev. X* **8**, 31087 (2018).
 24. Po, H. C., Zou, L., Vishwanath, A. & Senthil, T. Origin of Mott Insulating Behavior and Superconductivity in Twisted Bilayer Graphene. *Phys. Rev. X* **8**, 31089 (2018).
 25. Liu, J., Liu, J. & Dai, X. Pseudo Landau level representation of twisted bilayer graphene: Band topology and implications on the correlated insulating phase. *Phys. Rev. B* **99**, 1–9 (2019).
 26. Xie, M. & MacDonald, A. H. On the nature of the correlated insulator states in twisted bilayer graphene. Preprint at <https://arxiv.org/abs/1812.04213> (2018).
 27. Goodwin, Z. A. H., Corsetti, F., Mostofi, A. A. & Lischner, J. Twist-angle sensitivity of electron correlations in moiré graphene bilayers. *Phys. Rev. B* **100**, 121106 (2019).
 28. Kim, K. *et al.* Van der Waals Heterostructures with High Accuracy Rotational Alignment. *Nano Lett.* **16**, 1989–1995 (2016).
 29. Wong, D. *et al.* A modular ultra-high vacuum millikelvin scanning tunneling microscope. Preprint at <https://arxiv.org/abs/1910.08073> (2019).
 30. Li, G. *et al.* Observation of Van Hove singularities in twisted graphene layers. *Nat. Phys.* **6**, 109–113 (2010).
 31. Brihuega, I. *et al.* Unraveling the intrinsic and robust nature of van hove singularities in twisted bilayer graphene by scanning tunneling microscopy and theoretical analysis. *Phys. Rev. Lett.* **109**, 1–5 (2012).
 32. Wong, D. *et al.* Local spectroscopy of moiré-induced electronic structure in gate-tunable twisted bilayer graphene. *Phys. Rev. B* **92**, 31–36 (2015).
 33. Liu, J., Ma, Z., Gao, J. & Dai, X. Quantum Valley Hall Effect, Orbital Magnetism, and Anomalous Hall Effect in Twisted Multilayer Graphene Systems. *Phys. Rev. X* **9**, 31021 (2019).
 34. Bultinck, N., Chatterjee, S. & Zaletel, M. P. Anomalous Hall ferromagnetism in twisted bilayer graphene. Preprint at <https://arxiv.org/abs/1901.08110> (2019).
 35. Zhang, Y.-H., Mao, D. & Senthil, T. Twisted Bilayer Graphene Aligned with Hexagonal Boron Nitride: Anomalous Hall Effect and a Lattice Model. Preprint at

<https://arxiv.org/abs/1901.08209> (2019).

36. Kang, J. & Vafeek, O. Strong Coupling Phases of Partially Filled Twisted Bilayer Graphene Narrow Bands. *Phys. Rev. Lett.* **122**, 246401 (2019).
37. Li, G., Luican, A. & Andrei, E. Y. Self-navigation of a scanning tunneling microscope tip toward a micron-sized graphene sample. *Rev. Sci. Instrum.* **82**, (2011).
38. Huang, Y. *et al.* Reliable Exfoliation of Large-Area High-Quality Flakes of Graphene and Other Two-Dimensional Materials. *ACS Nano* **9**, 10612–10620 (2015).
39. Zhang, Y. *et al.* Giant phonon-induced conductance in scanning tunnelling spectroscopy of gate-tunable graphene. *Nat. Phys.* **4**, 627–630 (2008).
40. Velasco, J. *et al.* Nanoscale Control of Rewriteable Doping Patterns in Pristine Graphene/Boron Nitride Heterostructures. *Nano Lett.* **16**, 1620–1625 (2016).

Acknowledgements

We thank P. Jarillo-Herrero, E. Berg, A. Stern, A.H. MacDonald, B. Jäck, X. Liu, C.-L. Chiu, N.P. Ong, S. Wu, and S. Kahn for useful discussions. This work was primarily supported by the Gordon and Betty Moore Foundation as part of the EPiQS initiative (GBMF4530) and DOE-BES grant DE-FG02-07ER46419. Other support for the experimental work was provided by NSF-MRSEC through the Princeton Center for Complex Materials DMR-142054, NSF-DMR-1608848, ExxonMobil through the Andlinger Center for Energy and the Environment at Princeton, and the Princeton Catalysis Initiative. K.W. and T.T. acknowledge support from the Elemental Strategy Initiative conducted by the MEXT, Japan, A3 Foresight by JSPS and the CREST (JPMJCR15F3), JST. B.L. acknowledges support from the Princeton Center for Theoretical Science at Princeton University. B.A.B. acknowledges support from the Department of Energy DE-SC0016239, Simons Investigator Award, the Packard Foundation, the Schmidt Fund for Innovative Research, NSF EAGER grant DMR-1643312, and NSF-MRSEC DMR-1420541. AY acknowledges the hospitality of the Trinity College and Cavendish Laboratory in Cambridge, UK during the preparation of this manuscript, which was also funded in part by a

QuantEmX grant from the Institute for Complex Adaptive Matter and the Gordon and Betty Moore Foundation (GBMF5305).

Author Contributions

D.W., K.P.N., M.O., and A.Y. designed the research strategy, carried out STM/STS measurements, and performed the data analysis. D.W., M.O., and K.P.N fabricated samples. S.J., D.W., K.P.N., M.O., and A.Y. constructed the STM. K.W. and T.T. synthesized the h-BN crystals. B.L. and B.A.B. performed the theoretical calculations. All authors discussed the results and contributed to the writing of the manuscript.

Figure Captions:

Figure 1 | Cascade of transitions in spectroscopy on an AA site. **a**, Schematic of the experimental setup. **b**, STM topographic image of 1.06° MATBG ($V_b = -80$ mV, $I = 300$ pA). **c**, $dI/dV(V_b, V_g)$ measured at the center of an AA site (Initial tunneling parameters: $V_b = -100$ mV, $I = 1$ nA, 4.121 kHz sinusoidal modulation of $V_{rms} = 1$ mV). **d**, Same as **c** but divided by I/V_b . **e**, Cartoon schematic of features seen in **c** and **d**. **f**, dI/dV line cuts from $V_g = 31$ V to 13 V (left) and $V_g = -4$ V to -23 V (right). Triangles mark peaks corresponding to the features schematically depicted in **e**. Sequential curves are vertically offset by 2.5 nS (left) and 4 nS (right) for clarity.

Figure 2 | Theoretical model with on-site Hubbard repulsion U. **a**, Calculated spectral weight for a two-band Hubbard model with four flavors per band in the limit of vanishing hopping. The on-site interaction strength is $U = 23$ meV, the energy difference between the flat bands is $2E_0 = 16$ meV, and the temperature is $k_B T = 0.5$ meV. **b**, The features in **a** correspond to the on-site one-particle excitations schematically depicted here. The colored circles correspond to electrons

of different flavors, and the arrows represent different possible excitations. Each excitation has two possible energies depending on the value of the chemical potential (determined by the sign of δ). **c**, Schematic for the spectroscopic degeneracy (SD) versus energy (E) for various integer values of ν . The SD is determined by the number of excitations (arrows) in **b**, and the colors indicate the types of excitations depicted in **b**. **d**, The calculated chemical potential as a function of filling jumps by U at integer ν , except at the CNP where it jumps by $2E_0 + U$.

Figure 3 | Chemical potential observed through remote band oscillations. a, $dI/dV(V_b, V_g)$ measured at the center of an AB site at zero magnetic field (Initial tunneling parameters: $V_b = -100$ mV, $I = 1$ nA, 4.121 kHz sinusoidal modulation of $V_{\text{rms}} = 0.6$ mV). **b**, $dI/dV(V_b, V_g)$ measured at the center of an AB site at out-of-plane magnetic field $B_{\perp} = 9$ T (Initial tunneling parameters: $V_b = 100$ mV, $I = 0.6$ nA, 4.121 kHz sinusoidal modulation of $V_{\text{rms}} = 0.6$ mV). **c**, Onset energy of the conduction (pink) and valence (cyan) remote bands (RB) as a function of V_g extracted from data in **a** (solid lines) and in **b** (dotted lines). Curves are continuous at $\nu = 0$, but curves on the left and right panels were offset by different arbitrary energies for clarity. **d**, Chemical potential calculated from data in **c** using the mean-field model discussed in the text. Cusp-like features, which signify discontinuities in the electronic compressibility, are seen at each non-zero integer filling. As in **c**, curves are continuous at $\nu = 0$ but are offset by arbitrary energies for clarity. **e**, $dI/dV(V_b = 0 \text{ V}, V_g)$ from the data in **a** ($B_{\perp} = 0$ T; solid line) and **b** ($B_{\perp} = 9$ T; dotted line). At $B_{\perp} = 0$ T, dips in conductance are visible at each integer filling, denoted by the set of nine evenly spaced shaded bars.

Methods

STM measurements. All STM measurements were performed on a home-built, ultra-high vacuum (UHV) STM²⁹ near $T = 6$ K using a tungsten tip. The tip was prepared on a Cu(111) single crystal and calibrated against the crystal's characteristic Shockley surface state (see Extended Data Fig. 6 for details about why this is necessary). Graphene was electrostatically gated through a voltage V_g applied to a degenerately p-doped Si back-gate, while V_b was applied to the sample relative to the tip. Scanning tunneling spectroscopy (STS) measurements were obtained through lock-in detection of the tunneling current induced by a small sinusoidal modulation voltage added to the sample bias. The STM tip was navigated to graphene using a capacitance-based technique³⁷.

Sample preparation. Devices were prepared using a “tear-and-stack” method²⁸. The fabrication procedure for the device that yielded the data in Fig. 1 (“Device A”) is described here (see Extended Data Fig. 7 for a schematic). Transparent tape was pressed onto a glass slide. Two additional pieces of tape were placed on the slide parallel to the original tape and covering its edges to produce a channel running along the length of the glass slide. Polyvinyl alcohol (PVA, 5% by weight dissolved in water and filtered through a 0.2- μm pore-size PTFE syringe filter) was dropped onto the tape/glass slide. A separate glass slide was slid over the first glass slide to smooth out the PVA to the thickness of the channel. The PVA was allowed to dry in air for 15 minutes before the underlying transparent tape support was lifted from the glass slide. A 2 mm x 2 mm polydimethylsiloxane (PDMS, Sylgard 184) film was then placed between the PVA/tape and the glass slide to form the completed “PVA handle”. Using a transfer station, the PVA handle was aligned with h-BN (exfoliated on SiO_2), which was picked up by the PVA at 60 °C. The PVA handle was then aligned such that this h-BN flake contacted half of a monolayer

graphene sheet (exfoliated on piranha-cleaned SiO₂ using a hot cleave method³⁸). As the PVA handle was lifted, graphene adhered to h-BN where contacted and tore at the h-BN flake's edge. The remaining graphene, left on the SiO₂ wafer, was rotated by 1.3° with respect to the PVA handle, and the PVA handle was translated to pick up the rotated piece of graphene. Care was taken throughout this procedure to remove mechanical backlash in the transfer station's rotation stage, ensuring higher precision of this rotation angle. A polymethyl methacrylate (PMMA)/tape/PDMS/glass slide (the "PMMA handle") was prepared in a similar manner to the PVA handle, omitting the channel construction steps to produce a thinner film. Additionally, the PMMA handle was baked on a hot plate at 130 °C for 5 minutes. Using the transfer stage, the PVA handle was aligned and contacted to the PMMA handle. Water was injected between the two handles with a syringe, dissolving the PVA and transferring the graphene/h-BN stack to the PMMA handle. The PMMA handle was placed in three beakers of room-temperature water for 10 minutes each, further dissolving any remaining PVA residue. Using the transfer stage again, the graphene/h-BN heterostructure on the PMMA handle was pressed against SiO₂/Si with pre-patterned Au/Ti electrodes at 110° C. The graphene at the edge of the h-BN flake makes electrical contact to these pre-patterned electrodes. After this transfer, PMMA residue was dissolved by placing the completed device in dichloromethane (DCM) heated just below its boiling point for 25 minutes. The device was subsequently dipped in acetone, water, and isopropanol (IPA) for a few minutes. Finally, the device was annealed in UHV for 12 hours at 170 °C, followed by a 2 hour anneal at 400 °C. The fabrication of the device that yielded data for Fig. 3 ("Device B") is similar, except the unfiltered PVA concentration was increased to 25% by volume, the PMMA was eliminated from the procedure, only water was used as the final solvent,

the graphene was rotated by 1° during the tear-and-stack, and miscellaneous modifications were made to various temperatures and wait times.

Theoretical calculations. The zero-hopping-limit spectral weight in Fig. 2a was calculated by considering two orbitals at single-particle energies $\pm E_0$ corresponding to the two flat bands of MATBG. Each orbital has a 4-fold spin and valley degeneracy. At zero hopping, each site is decoupled from the others. The single-site Hamiltonian is given by

$$H = E_0(n_2 - n_1) + \frac{U}{2}n(n - 1)$$

where $0 \leq n_\alpha \leq 4$ is the number of electrons in orbital α ($\alpha = 1, 2$), and $n = n_1 + n_2$ is the total number of electrons on an AA site. The spectral weight at temperature T and chemical potential μ is given by

$$A(\omega) = Z^{-1} \sum_{l,m} \delta(\omega - \epsilon_l + \epsilon_m) (e^{-\beta\epsilon_m} + e^{-\beta\epsilon_l}) |\langle l | c_{\alpha,f}^\dagger | m \rangle|^2$$

where $Z = \text{tr } e^{-\beta(H-\mu n)}$ is the partition function ($\beta = 1/k_B T$), ϵ_m and $|m\rangle$ are the energy and wavefunction of the m -th eigenstate of $H - \mu n$, and $c_{\alpha,f}^\dagger$ is the electron creation operator of orbital α ($\alpha = 1, 2$) and spin/valley flavor f ($1 \leq f \leq 4$). The average electron filling can be calculated by $\nu = \langle n \rangle - 4 = \frac{\partial \ln Z}{\partial \mu} - 4$ (note that $\langle n \rangle = 4$ at the CNP), which is valid for $|\nu| \leq 4$.

Here we set $U = 23$ meV, $E_0 = 8$ meV, and $k_B T = 0.5$ meV. We then plotted the spectral weight as a function of the energy bias ω and the average filling ν , and the chemical potential μ was plotted as a function of ν . To simulate the remote band contribution, we assumed $\mu = \pm[\Delta + D^{-1}(|\nu| - 4)]$ for filling $|\nu| \geq 4$ (\pm signs for electron side and hole side, respectively), where Δ (set to 15 meV in the calculations) is the gap from the flat band to the remote band, and D is the DOS of the remote band. From the definition of spectral weight, the contribution of one-

particle excitations from a state with energy ϵ_l is reduced by $e^{-\beta(\epsilon_l - \epsilon_0)}$, where ϵ_0 is the ground-state energy. This exponentially suppresses any spectral weight beyond energy U (or $U + 2E_0$ at the CNP).

For Extended Data Fig. 3, we performed exact diagonalization (ED) of a toy Hubbard model of two nearly flat bands with 2-fold degeneracy. The model is defined on a 2×2 periodic triangular lattice (4 sites in total, representing the lattice of AA stacking sites) with two 2-fold degenerate orbitals (i.e. 4 orbitals in total) per site, respectively. The Hamiltonian is given by

$$H = \sum_i \left[E_0 (n_{2,i} - n_{1,i}) + \frac{U}{2} n_i (n_i - 1) \right] + t \sum_{\langle ij \rangle} \sum_{f=1,2} (c_{1,f,i}^\dagger c_{1,f,j} + c_{2,f,i}^\dagger c_{2,f,j} + h.c.)$$

where i runs over sites, $\langle ij \rangle$ represents nearest neighbors, $f = 1, 2$ is the flavor index, $n_{\alpha,i} = \sum_{f=1,2} c_{\alpha,f,i}^\dagger c_{\alpha,f,i}$ is the number of electrons in orbital α ($\alpha = 1, 2$) at site i , and $n_i = n_{1,i} + n_{2,i}$ is the total number of electrons at site i . Extended Data Fig. 3a is the zero-temperature spectral weight on a particular site for all possible fillings. The chemical potential $\mu = dE_{gs}(N)/dN$ is determined by the ground state energy $E_{gs}(N)$ as a function of the total electron number of the lattice $N = \sum_i n_i$. We set $U = 23$ meV, $E_0 = 8$ meV, and $t = 0.6$ meV. When both flat bands are fully empty or fully occupied, and E_F is in the remote band, we assume the spectral weight only shifts in bias linearly with respect to the electron filling, with slopes determined by the DOS of the remote bands.

To extract the remote band onset energies $E_{R+(-)}(v)$, we analyzed spectra $dI/dV(V_b, V_g)$ at each gate voltage V_g individually. For each bias voltage V_b of this spectrum, we obtain a quantity $f(V_b)$ by performing linear regressions via a least-squares method on the spectrum in two domains ($[V_b, V_b + \Delta V]$ and $[V_b - \Delta V, V_b]$, where ΔV is dependent on the gate voltage of the spectrum) and then subtracting the slopes obtained from these regressions. Local maxima of this

function $f(V_b)$ occur when the slope of the spectrum discontinuously jumps at the onset of one of the remote bands. A list of these maxima and their associated gate voltages produces the data plotted in Fig. 3c, which has been averaged over a sliding window of width $\Delta V_g = 3$ V. Our mean-field model assumes a form for these onset energies $E_{R+(-)}(\nu) = \Delta_{R+(-)} + \nu U' - \mu(\nu)$. As ν increases by 1, the chemical potential increases by U , and the mean-field interaction term increases by U' . The peak-to-peak energy separation of neighboring cusps of $E_{R+(-)}(\nu)$ has a value $U - U' \approx 8$ meV, estimated from the most prominent cusps visible in Fig. 3a. Using the measured value $U = 23$ meV obtained by the extent of the cascade features, we estimate a value $U' \approx 15$ meV and solve for $\Delta\mu(\nu) = \nu U' - E_{R+(-)}(\nu)$ (which is plotted in Fig. 3d).

Data Availability

The data that supports the findings of this study are available from the corresponding author upon reasonable request.

Competing Interests

The authors declare no competing interests.

Extended Data Figure Captions:

Extended Data Figure 1 | dI/dV curves on an AA site. **a**, Optical micrograph of MATBG/h-BN device from which data in main text Fig. 1 were acquired (Device A). The white dashed line encloses the MATBG area. **b**, STM topographic image of 1.06° MATBG ($V_b = -500$ mV, $I = 10$ pA). **c**, dI/dV spectra acquired at the center of an AA site, where both flat bands are completely filled (red), the valence flat band is filled but the conduction flat band is empty (purple), and both flat bands are completely empty (blue). These data were acquired on the same AA site as that shown in main text Fig. 1c. Sequential curves are vertically offset by 20 nS for clarity. **d**, Same as **c** but for more gate voltages ($V_g = 50$ V to -50 V). Sequential curves are vertically offset by 2.5 nS for clarity. A feature due to inelastic tunneling is sometimes seen at $V_b = \pm 60$ mV but has no influence on observations closer to E_F than ± 60 mV³⁹. **e**, $-dE_H/dV_g$ as a function of gate voltage (rolling average over a $\Delta V_g = 0.65$ V window) obtained by extracting the energy E_H of the peak in dI/dV for the cascade features shown in main text Fig. 1. Upward pointing triangles identify discontinuous transitions between each cascade feature in the conduction flat band (red), around charge neutrality (purple), and in the valence flat band (blue). **f**, $dI/dV(V_b = 0$ V, $V_g)$ on the AA site. Equally spaced shaded bars are drawn over dips in the zero-bias conductance, which allow us to identify each integer filling ν of the flat bands. Zero-bias conductance peaks are marked by downward pointing triangles, which can be attributed to each of the discontinuities in **a**.

Extended Data Figure 2 | Cascade features at other angles near the magic angle. The cascade features that we report in this manuscript were reproduced 8 times in Device A and 7 times in Device B (all angles between 0.97° and 1.17°). Each observation can be regarded as

independent because (i) the STM tip is different between each measurement and (ii) the local twist angle is different between each measurement due to large spatial inhomogeneity in each device. A small moiré between graphene and h-BN (varying around 8°) was often seen in Device A, while no graphene/h-BN moiré was seen in Device B. Here, **a-d** along with main text Fig. 1c-d show our first five observations of the cascade features in Device A. **a**, The left panel shows $dI/dV(V_b, V_g)$ measured at the center of an AA site, while the right panel shows the same quantity divided by I/V_b . The twist angle is 1.01° with 0.2% strain (Initial tunneling parameters: $V_b = -300$ mV, $I = 0.3$ nA, 551.7 Hz sinusoidal modulation of $V_{\text{rms}} = 1$ mV). **b**, Same as **a** for a twist angle of 0.97° and 0% strain (Initial tunneling parameters: $V_b = -80$ mV, $I = 1.0$ nA, 4.117 kHz sinusoidal modulation of $V_{\text{rms}} = 0.3$ mV). **c**, Same as **a** for a twist angle of 1.03° and 0.2% strain (Initial tunneling parameters: $V_b = -100$ mV, $I = 0.5$ nA, 4.121 kHz sinusoidal modulation of $V_{\text{rms}} = 1.0$ mV). **d**, Same as **a** for a twist angle of 1.07° and 0.1% strain (Initial tunneling parameters: $V_b = -80$ mV, $I = 1.0$ nA, 4.121 kHz sinusoidal modulation of $V_{\text{rms}} = 1.0$ mV). Twist angles are measured within $\pm 0.01^\circ$.

Extended Data Figure 3 | Exact diagonalization. **a**, Theoretical spectral weight for different values of the filling ν calculated by exact diagonalization of the two-flavor, two-band Hubbard model consisting of 4 sites, interband separation $2E_0 = 16$ meV, nearest-neighbor hopping $t = 0.6$ meV, and on-site Coulomb repulsion $U = 23$ meV. Dashed black lines highlight the cascade features, which are fewer in number than in the experimental data because the theoretical model has only 2 flavors (compared to fourfold degeneracy in MATBG). **b**, The calculated chemical potential as a function of ν shows jumps at integer fillings. The inset schematically depicts the 4

AA sites, with on-site repulsion U and hopping t . **c**, Calculated energy difference between cascade features and the chemical potential jump at $\nu = 1$ as a function of U .

Extended Data Figure 4 | Undertwisted and overtwisted bilayer graphene. **a**, $dI/dV(V_b, V_g)$ measured at the center of an AA site for 0.85° (0.3% strain) twisted bilayer graphene (Device B; Initial tunneling parameters: $V_b = -40$ mV, $I = 30$ pA, 381.7 Hz sinusoidal modulation of $V_{rms} = 1.2$ mV). These data do not show the cascade features. **b**, $dI/dV(V_b, V_g)$ measured at the center of an AA site for 1.21° (0.2% strain) twisted bilayer graphene (Device A; Initial tunneling parameters: $V_b = -100$ mV, $I = 1.5$ nA, 4.121 kHz sinusoidal modulation of $V_{rms} = 0.5$ mV). These data do not show the cascade features (except possibly very faintly in the valence flat band). A dip of unknown origin at E_F is visible at all carrier densities. The persistence of this dip disqualifies it from being a superconducting or correlated-insulating gap. This dip is likely a Coulomb gap or a tip artifact⁷.

Extended Data Figure 5 | dI/dV curves on an AB site. dI/dV spectra acquired at the center of an AB region in 1.05° MATBG on Device B ($V_g = 38$ V to -40 V). These data are the same as shown in main text Fig. 3a and clearly show gate-dependent oscillations in the remote bands. Sequential curves are vertically offset by 1 nS for clarity.

Extended Data Figure 6 | Tip-induced collapse of flat band. Measurements on MATBG can strongly depend on the STM tip, so we calibrate the tip against the Shockley surface state of Cu(111). Damage to or contamination of the tip causes distortions to observed features. Copper and tungsten, incidentally, have work functions similar to graphene. **a**, $dI/dV(V_b, V_g)$ measured at

the center of an AA site in Device A, with a twist angle of 1.01° and 0.2% strain (same data as Extended Data Fig. 2a). The lack of symmetry in $dI/dV(V_b, V_g)$ indicates that the tip condition is already nonoptimal. **b**, Same as **a** after lightly crashing the tip into the sample (Initial tunneling parameters: $V_b = -200$ mV, $I = 0.5$ nA, 551.7 Hz sinusoidal modulation of $V_{\text{rms}} = 1$ mV). The crash further degraded the tip, causing the valence flat band to appear to cross E_F without pinning. This can be caused by changes in tip-induced band bending⁷ and tip-induced doping⁴⁰.

Extended Data Figure 7 | Device fabrication. **a**, Schematic showing step-by-step device fabrication procedure for Device A (Device B is similar, but without PMMA). **b**, In order to do STM measurements, MATBG must be “face up.” To achieve this, we transfer a MATBG/h-BN stack from its initial PVA handle to a secondary handle. Water injected between the two glass handles via a syringe dissolves the PVA. **c**, 500×500 nm² STM topograph of Device B showing a moiré pattern and physical corrugation in the underlying substrate ($V_b = -400$ mV, $I = 100$ pA). **d**, Zoomed-in image of the center of the area in **c**.

FIGURE 1

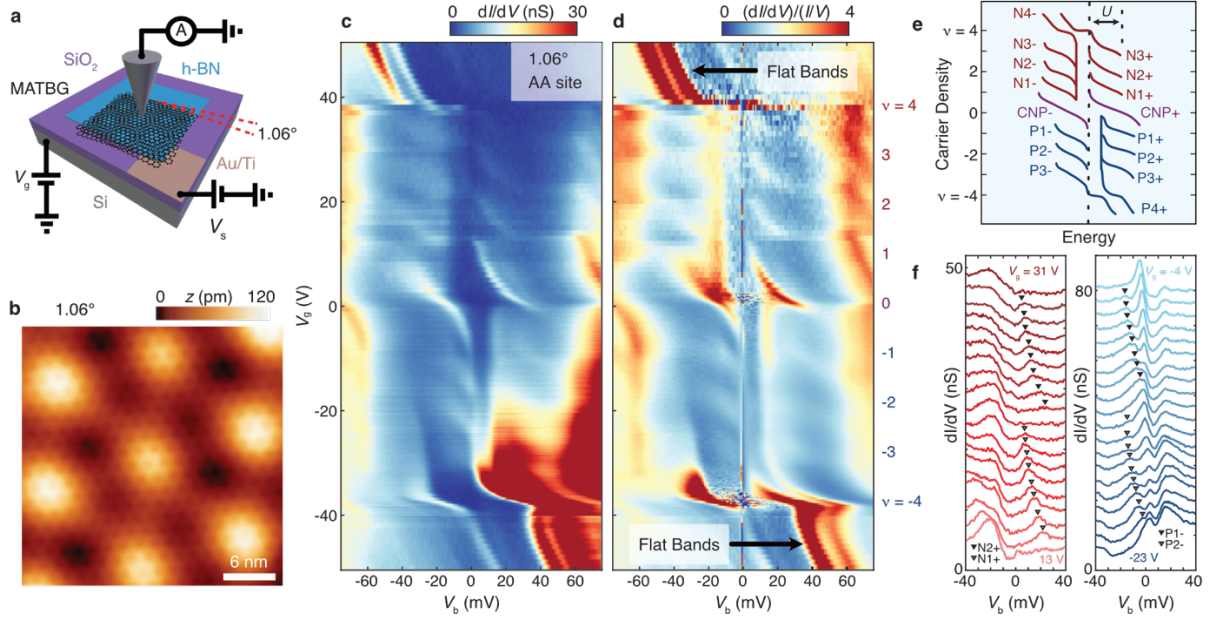


FIGURE 2

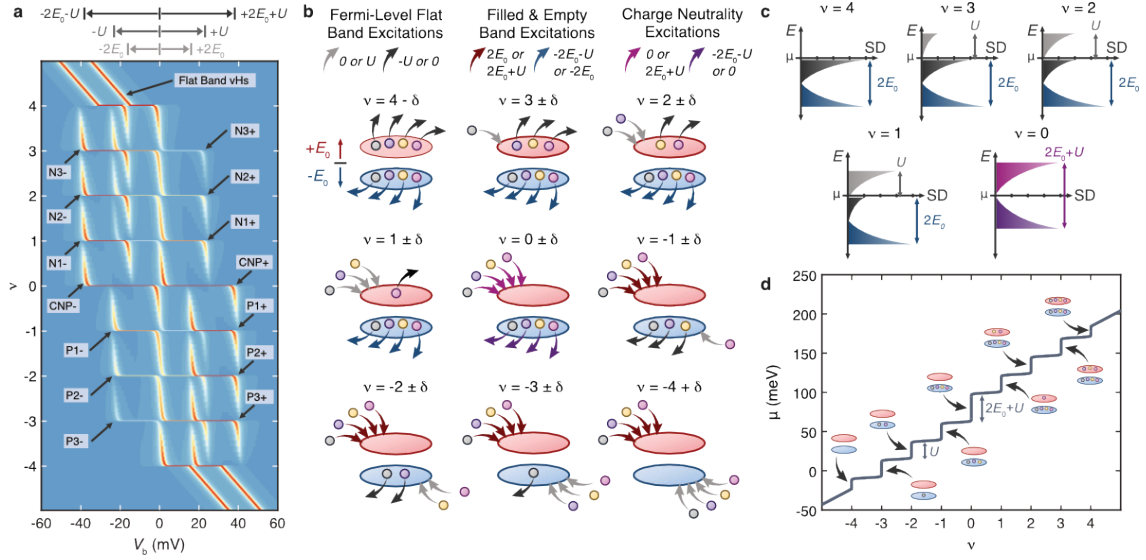
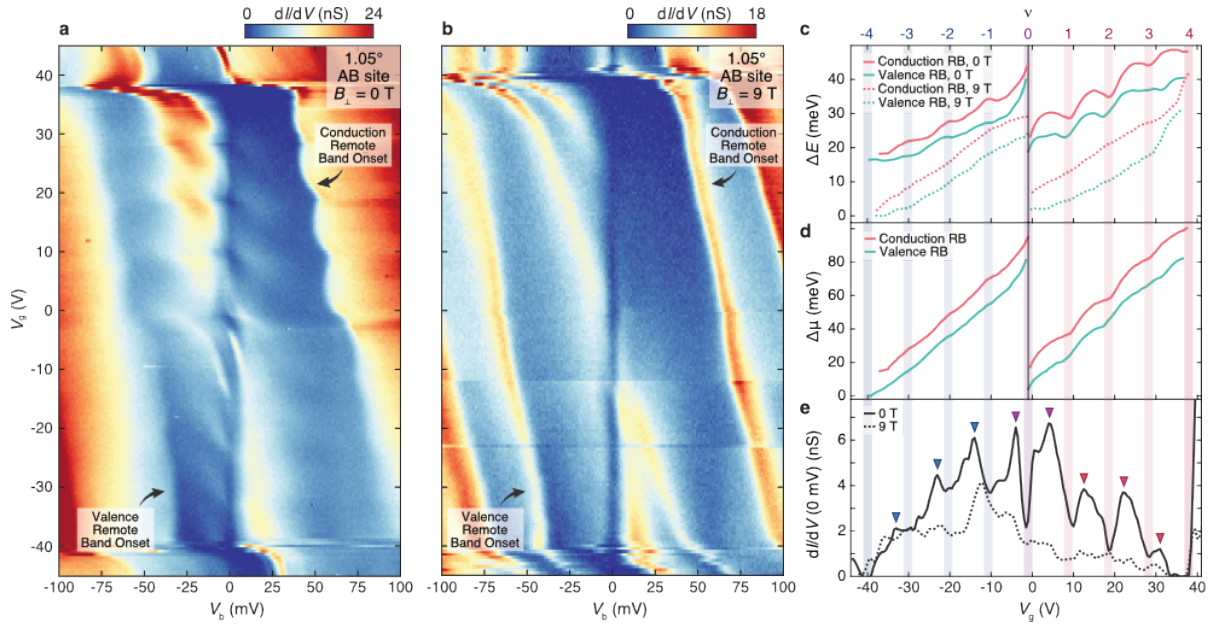
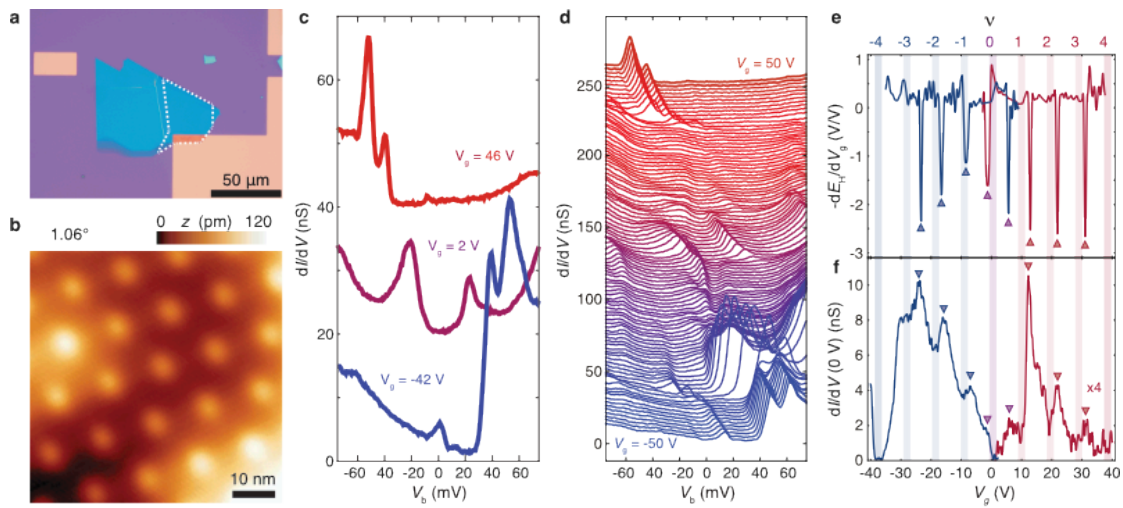


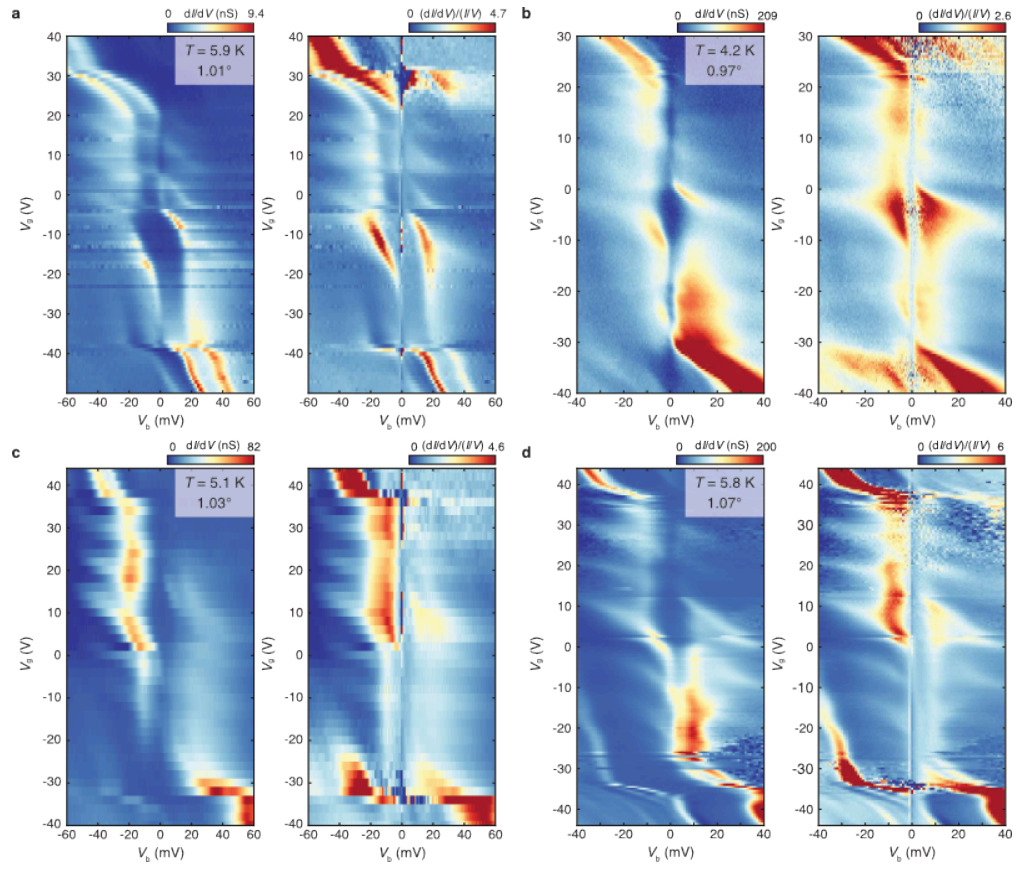
FIGURE 3



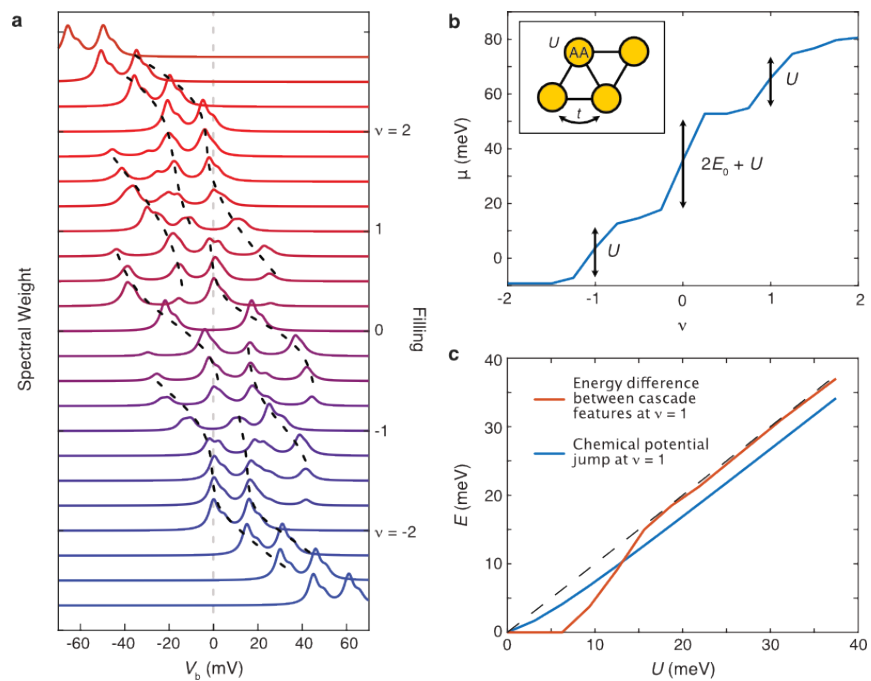
EXTENDED DATA FIGURE 1



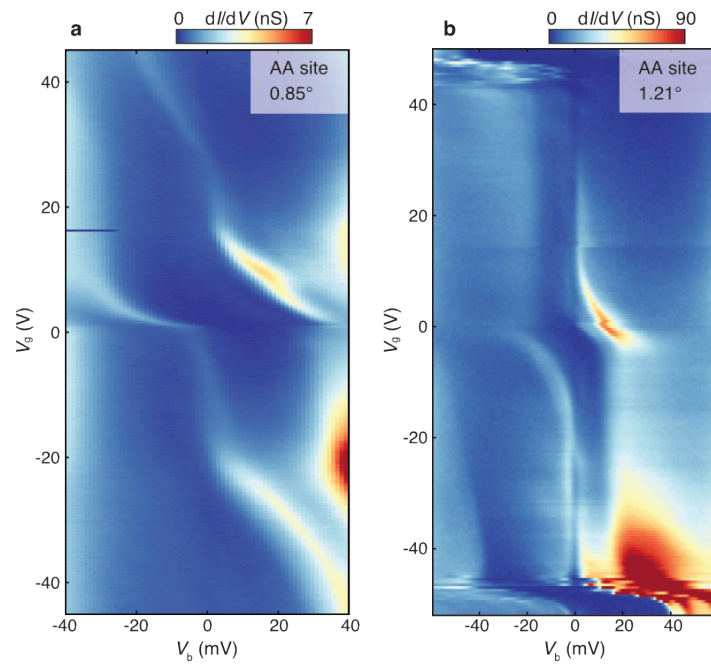
EXTENDED DATA FIGURE 2



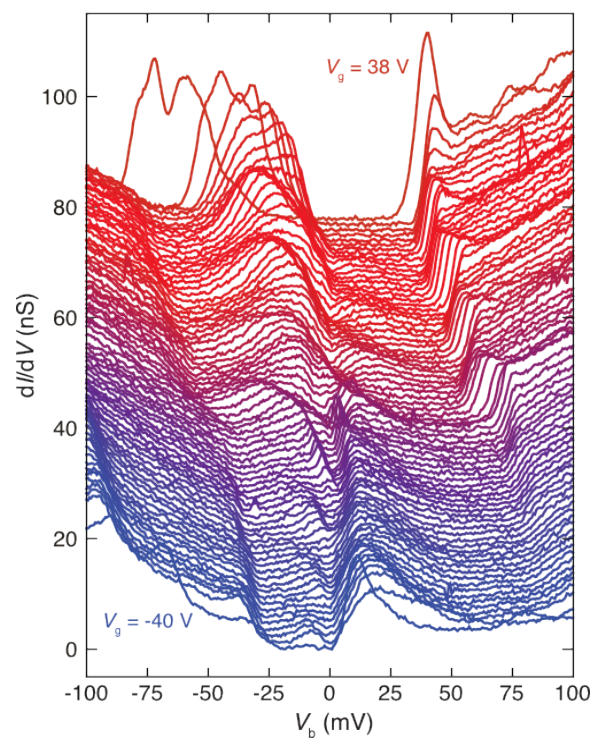
EXTENDED DATA FIGURE 3



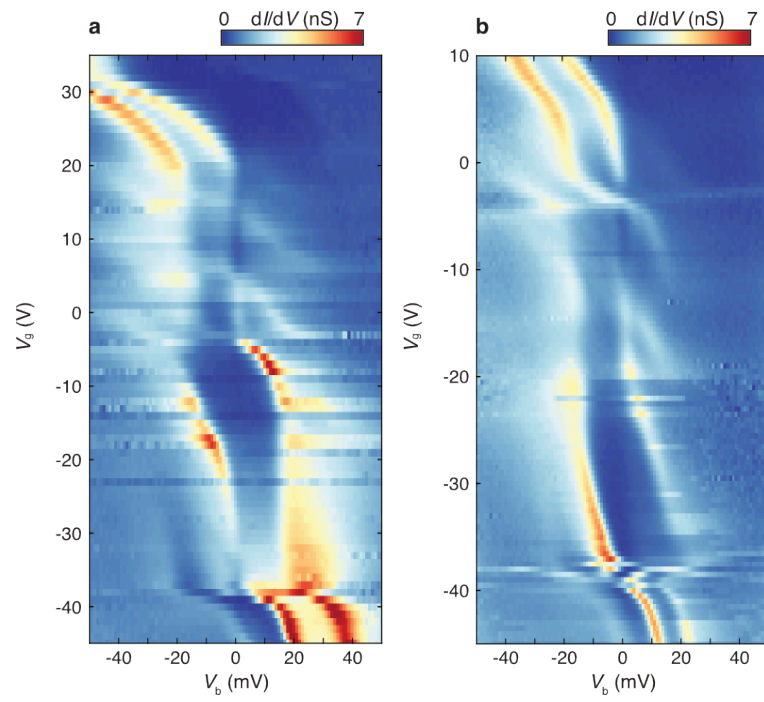
EXTENDED DATA FIGURE 4



EXTENDED DATA FIGURE 5



EXTENDED DATA FIGURE 6



EXTENDED DATA FIGURE 7

